IOP Publishing Smart Materials and Structures
Smart Mater. Struct. 26 (2017) 035009 (10pp) doi:10.1088/1361-665X/aa5496

Design of flat pneumatic artificial muscles

Jackson Wirekoh[1] **and Yong-Lae Park**[2,3]

[1] Mechanical Engineering, Carnegie Mellon University, Pittsburgh, PA 15213, USA
[2] Robotics Institute, Carnegie Mellon University, Pittsburgh, PA 15232, USA
[3] Mechanical and Aerospace Engineering, Seoul National University, Seoul, 08826, Korea

E-mail: ylpark@cs.cmu.edu

Received 22 July 2016, revised 14 December 2016
Accepted for publication 19 December 2016
Published 7 February 2017

Abstract

Pneumatic artificial muscles (PAMs) have gained wide use in the field of robotics due to their ability to generate linear forces and motions with a simple mechanism, while remaining lightweight and compact. However, PAMs are limited by their traditional cylindrical form factors, which must increase radially to improve contraction force generation. Additionally, this form factor results in overly complicated fabrication processes when embedded fibers and sensor elements are required to provide efficient actuation and control of the PAMs while minimizing the bulkiness of the overall robotic system. In order to overcome these limitations, a flat two-dimensional PAM capable of being fabricated using a simple layered manufacturing process was created. Furthermore, a theoretical model was developed using Von Karman's formulation for large deformations and the energy methods. Experimental characterizations of two different types of PAMs, a single-cell unit and a multi-cell unit, were performed to measure the maximum contraction lengths and forces at input pressures ranging from 0 to 150 kPa. Experimental data were then used to verify the fidelity of the theoretical model.

Keywords: pneumatic artificial muscle (PAM), soft robotics, design and manufacturing, embedded fibers, stress–strain test, actuators

(Some figures may appear in colour only in the online journal)

1. Introduction

Pneumatic artificial muscles (PAMs) have been widely used in the field of robotics, especially for soft robotic applications, due to their ability to produce linear forces and displacements with a simple mechanism [1–3]. In most cases, these actuators are composed of elastomeric cylindrical bladders geometrically constrained by flexible yet inextensible mechanisms such as meshes [1, 2, 4], nets [5], and embedded fibers [6, 7]. These systems work in unison producing compact, lightweight, and compliant actuators capable of high force generation to weight ratios [1–3]. In addition, due to the use of compressed air for actuation, soft robotic systems with PAMs have almost no danger when compared with ones that use combustion or fire as a power source [8, 9]. These qualities have made PAMs a growing topic of interest among researchers and industry alike.

Modern research into the design and utilization of PAMs began with a McKibben-type actuator, which was first proposed by atomic physicist Joseph Laws McKibben in the late 1950's [1]. The McKibben actuator, which makes use of a braided mesh and cylindrical bladder to provide linear force and contraction when stimulated with pressurized air, was originally designed for use in an orthotic device to aid polio patients [1, 3, 10]. In later years, as pneumatic technology improved, companies such as Bridgestone Co. and Festo AG, modified and commercialized the McKibben design for use in robotic systems [1, 3, 10]. The success of the McKibben-type actuators resulted in further innovation and implementation of PAMs.

One such innovation was the Baldwin-type actuator first proposed in 1969, which later served as inspiration to actuators developed by Park *et al* [7]. This PAM design was composed of a thin cylindrical substrate with embedded glass filaments (fibers) that generally resulted in mechanical performances with reduced hysteresis when compared to that of McKibben-type actuators [3]. However, radial expansion limited the maximum input pressures to 100 kPa [3]. Another notable design, conceptualized and produced by Daerden and Lefeber in 2001, was the pleated pneumatic artificial muscle (PPAM) [10]. This design was created as a more robust PAM

capable of addressing the energy loss and hysteresis typically found in McKibben-type actuators. The PPAM is composed of a high-tensile-modulus cylindrical membrane that is folded in on itself (pleated) like the bellows of an accordion [10]. During operation, instead of wasting energy to radially deform, the PPAM's membrane simply unfurls, allowing the actuator to bulge out radially but shorten axially.

In addition to the aforementioned PAMs, polylobe and prolated designs, such as Robotic Muscle Actuators [3] and Yarlett-type actuators [3], respectively, have been created to produce linear motions. However, these actuators are uncommon in real world applications due to their complex designs. The McKibben-type actuator, Baldwin actuator, and PPAM, on the other hand, have traditionally seen wider use in both research and industry. However, their effectiveness, particularly relating to their use in wearable devices, is limited by their cylindrical form factors, as shown in a soft ankle orthotic device that used McKibben PAMs for actuation [11]. More specifically, due to the scaling of force generation with the radius of traditional PAMs, actuators become increasingly less compact when larger forces are desired. This prevents the design of streamlined wearable devices, which may limit the range of motion of the wearer.

Moreover, the nonlinear response of PAMs to input stimulation (i.e. air pressure) is a critical issue that must be addressed by designers during controlled device operation. In order to ensure effective real-time control of the actuators, while preserving the compactness and compliance of the system, researchers have attempted to integrate sensors directly in the PAMs during fabrication either by embedding conductive elements in the elastomeric air chamber for resistive sensing [7, 12, 13] or by adding braided conductive wires to the outer mesh structure for inductive sensing [14, 15]. However, due to the cylindrical form factor of the PAMs, the fabrication process becomes overly complicated. This complexity increases the difficulty of embedding multiple sensor elements for multimodal detection (e.g. position and force), which are necessary to effectively control the system.

In order to address the shortcomings of traditional cylindrical PAMs, a two-dimensional (2D) flat pneumatic artificial muscle (FPAM) is proposed. This study focuses on the design and theoretical modeling of the FPAMs. Furthermore, the proposed flat muscle design was realized through a simple layered fabrication method, and the theoretical model was experimentally verified. The remainder of the study is organized as follows: section 2 details the design and fabrication of the FPAM; section 3 discusses development of a theoretical model for the FPAM, section 4 details the experimental setup; section 5 provides analysis of experimental results, and section 6 discusses the conclusion.

2. Design and fabrication

A 2D FPAM, shown in figures 1 and 2, was designed to remain compact and easily predisposed to the addition of multiple

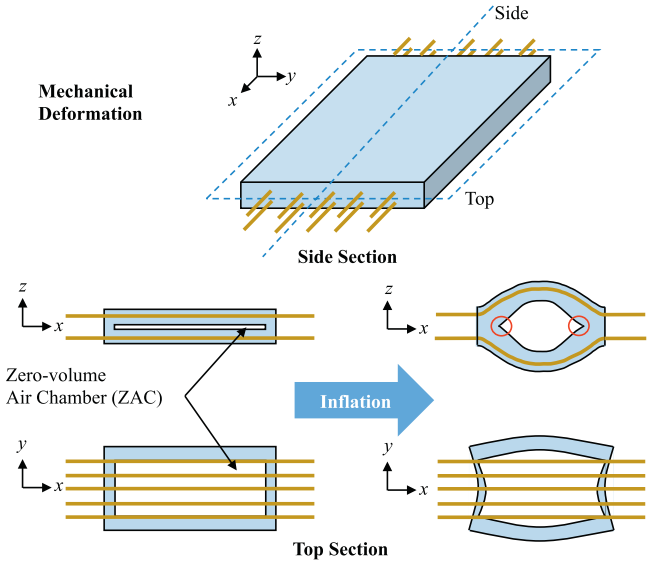

Figure 1. Illustration of actuator at rest (left) and sectional views of actuator at rest and inflated (right). Kevlar Fibers are shown in dark orange. Red circles indicate high stress concentrations.

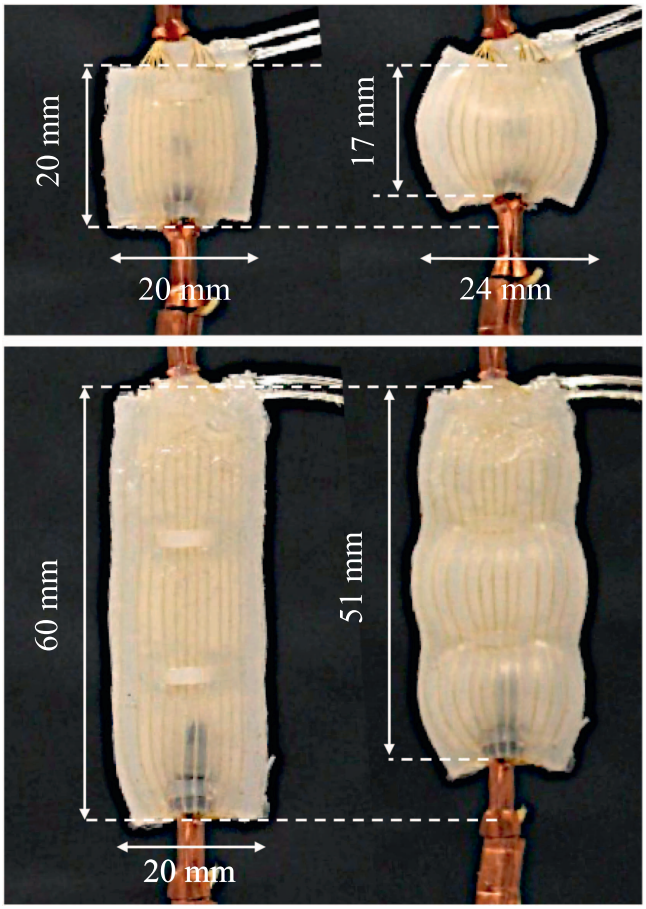

Figure 2. Prototypes of single cell unit at rest and contracted (top) and multi-cell unit (3 × 1 series) at rest and contracted (bottom). Prototypes experienced maximum thickness (out of plane) changes of 8 mm during contraction.

embedded sensor layers, which is very difficult to achieve when employing the cylindrical shape of traditional PAMs. This unusual form factor allows for the introduction of a concept described as the 'zero-volume air chamber' or ZAC [16], which manifests itself as a very thin ($\leqslant$0.1 mm) rectangular air volume encased by two flat elastomeric sheets. This design effectively reduces the overall thickness of the actuator by removing the necessity of having a designated air void in the center of the relaxed actuator as seen in typical PAMs. Furthermore, the flat configuration of the actuator makes it possible to easily resize and reconfigure each individual muscle array [16], which can be seen in figure 2. These features of the proposed 2D form factor will make it particularly easy to hide and/or incorporate the flat muscle into clothing-like wearable devices. In these applications, the 2D form factor becomes increasingly more important, particularly when larger forces are required despite the need to maintain the compactness of the system. Whereas for traditional cylindrical PAMs, in which the radius must be increased to generate larger forces (volumetric increase), the FPAM must only be designed with a wider air volume (area increase), which is tantamount to adding actuators in parallel. Therefore in situations in which covering a wider surface area is allowable, the FPAM offers minimal volumetric change while providing desired forces. These features will ultimately allow for wearables that look like elastic suits which are capable of naturally deforming with the human body while providing active assistance to body motions.

The FPAM proposed in this study is made of a silicone substrate that contains embedded Kevlar fibers. The stretchability of the substrate and the flexible yet inextensible nature of the fibers work in unison to produce axial contraction when the FPAM is pressurized and radially inflated, as shown in figure 1. However, the inflated actuator is subject to high stress concentrations along the sides of the bladder, which previously resulted in a prominent delamination failure mode along the edges [16]. To overcome this issue, a new fabrication process was proposed.

Illustrated in figures 3 and 4, the fabrication process makes use of uncured liquid silicone (Dragon Skin10, Smooth-On) and 3D printed molds to create two thin silicone sheets and a core (central substrate containing the ZAC) with an embedded water-soluble mask made of a water-soluble fabric stabilizer (Paper Solvy, Sulky). After curing, the silicone layers are stacked and adhered together to form the base actuator in the following order: bottom layer, aligned Kevlar fibers, core, aligned Kevlar fibers, and top layer. Finally, the mask is removed by water and tube fittings and securements for the Kevlar fibers are added to complete the actuator. Prototypes of the single cell unit (SCU) as well as a 3 $\times$ 1 multi-cell unit (MCU) are shown in figure 2. The SCU is 20 mm $\times$ 20 mm $\times$ 4 mm thick, while the MCU is 60 mm $\times$ 20 mm $\times$ 4 mm thick. Both actuators have ZAC dimensions of 14 mm $\times$ 14 mm $\times$ 0.1 mm thick.

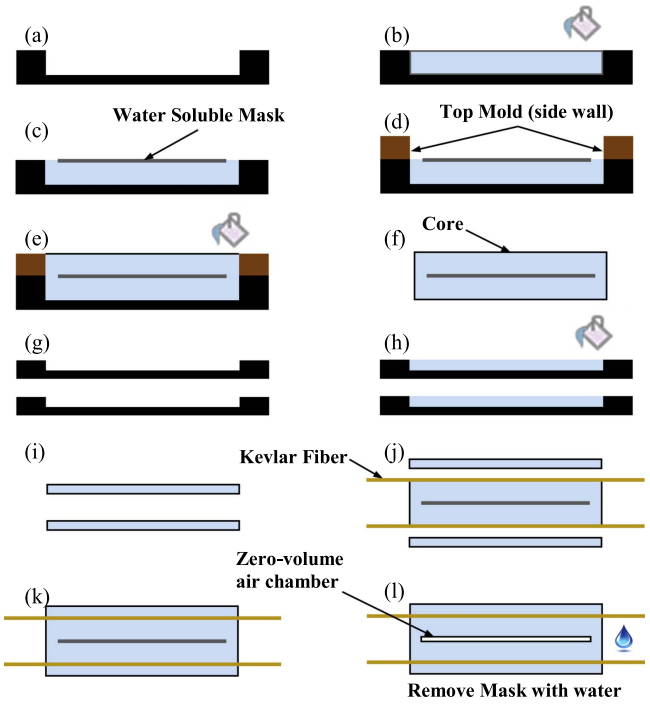

Figure 3. Fabrication process of FPAM using water-soluble mask: (a) prepare bottom core mold, (b) pour liquid elastomer for bottom half of core, (c) place water-soluble mask, (d) place top mold, (e) pour liquid elastomer for top half of core, (f) remove core after curing, (g) prepare thin layer molds, (h) pour liquid elastomer to create thin outer layers, (i) remove thin outer layers after curing, (j) align Kevlar, outer layers, and core, (k) bond using liquid elastomer, and (l) remove mask using water.

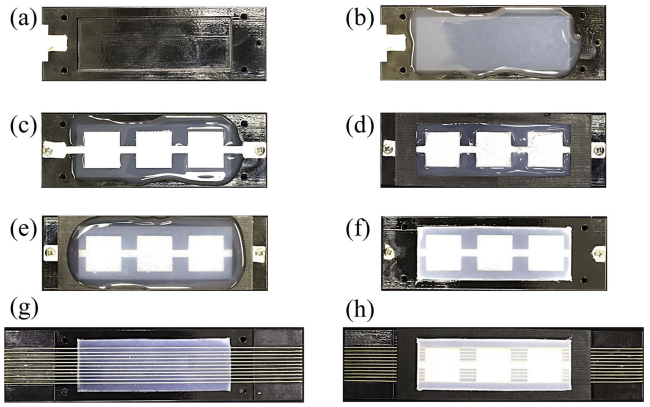

Figure 4. Photos of actual fabrication steps for 3 $\times$ 1 multi-cell FPAM: (a) bottom core mold (figure 3(a)), (b) liquid silicone in bottom core mold (figure 3(b)), (c) water-soluble mask on liquid silicone (figure 3(c)), (d) top mold added (figure 3(d)), (e) liquid silicone on mask (figure 3(e)), (f) cured core (figure 3(f)), (g) Kevlar fibers on cured bottom outer layer (figures 3(i) and (j)), and (h) core bonded to Kevlar fibers and bottom outer layer (figures 3(j) and (k)). (g) and (h) are repeated to complete prototype with top outer layer and Kevlar fibers.

3. Theory

A theoretical model was developed to approximate the properties of the proposed FPAM by assuming the actuator is composed of two flat rectangular composite sheets that are simply supported along the edges. Through this convention, modeling techniques for the large deformation of membranes (thickness small in comparison to length and width) [17–19] could be utilized.

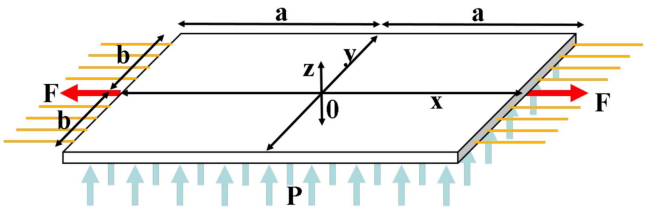

Figure 5. Approximation of top half of actuator as flat sheet under external force F and pressure P.

Figure 5 depicts the top half of the actuator with dimensions of $2a$ and $2b$, which are equal to the length and width of the air volume respectively. The membranes are subjected to an axial force F (required force to counteract contractive force of FPAM) in the x-coordinate direction at the loaded edges $x = \pm a$ and a uniformly applied lateral pressure P in the z-coordinate direction. In addition, the following assumptions are made regarding the deformation of the membranes:

1. Stress in the z-axis direction is considered negligible in comparison to x- and y- axes (σ_x, σ_y only).
2. The normal to midplane is normal after deformation (γ_{xy} only).
3. Deformation occurs in elastic range (Hooke's Law).
4. Bending strains are negligible in elastic range.
5. There is no delamination between fibers and elastic substrate, and
6. z-axis deflection is $w(x, y) = w_0 \cos\frac{\pi x}{2a} \cos\frac{\pi y}{2b}$ as postulated by Timoshenko [17, 18].

These assumptions were then applied to Von Karman's formulation for large deformations, provided in equations (1) and (2) as follows:

$$\nabla^4 \phi = E\left[\left(\frac{\delta^2 w}{\delta x \delta y}\right)^2 - \frac{\delta^2 w}{\delta x^2}\frac{\delta^2 w}{\delta y^2}\right], \tag{1}$$

$$\nabla^4 w = \frac{h}{D}\left[\frac{P}{h} + \frac{\delta^2\phi}{\delta y^2}\frac{\delta^2 w}{\delta x^2} + \frac{\delta^2\phi}{\delta x^2}\frac{\delta^2 w}{\delta y} - 2\frac{\delta^2\phi}{\delta x \delta y}\frac{\delta^2 w}{\delta x \delta y}\right], \tag{2}$$

where $\nabla^4 = \frac{\delta^4}{\delta x^4} + 2\frac{\delta^4}{\delta x^2 \delta y^2} + \frac{\delta^4}{\delta y^4}$, h is the thickness of the membrane, E is the Young's modulus, D is the structural rigidity, and Φ is the stress function defined by:

$$\sigma_x = \frac{\delta^2\phi}{\delta y^2}, \tag{a}$$

$$\sigma_x = \frac{\delta^2\phi}{\delta y^2}, \tag{b}$$

$$\tau_{xy} = -\frac{\delta^2\phi}{\delta y^2}. \tag{c}$$

Due to the difficulty in analytically solving equation (2), application of the energy methods [17–19], which will be detailed later, was used to solve for the unknown quantity w_0. Once solved, these formulations determined solutions for the x-axis and y-axis displacements $u(x, y)$ and $v(x, y)$. However, due to the nature of the membrane as an anisotropic composite, the directional dependence of the material properties had to be incorporated into the formulations. This is achieved through a reformulation of equation (1). Initially, the stress–strain relationship of the membrane was examined using Hooke's Law. This elastic (linear) relationship further simplifies these complex equations, while providing a powerful means for the development of solutions in both the plastic and hyperelastic (nonlinear) regime of deformations through the use of Ilyushin's iterative elastic solutions method [19], which is further expanded later in this section. Through this formulation, with the applied assumptions, the stress–strain relationships were defined as the following:

$$\varepsilon_x = \frac{1}{E_x}(\sigma_x - \nu_{xy}\sigma_y), \tag{3a}$$

$$\varepsilon_y = \frac{1}{E_y}(\sigma_y - \nu_{yx}\sigma_x), \tag{3b}$$

$$\gamma_{xy} = \frac{1}{G_{xy}}\tau_{xy}, \tag{3c}$$

where ε_x, ε_y, and γ_{xy} are the normal strains and the shear strain, respectively, σ_x, σ_y, and τ_{xy} are the normal stresses and the shear stress, respectively, E_x and E_y *are* the elastic moduli in the x- and y-axis directions, respectively, G_{xy} is the shear modulus, ν_{xy} is the Poisson's ratio representing the effects of y-axis stress on the x-axis deformation, and ν_{yx} is the Poisson's ratio representing the effects of x-axis stress on the y-axis deformation. Approximations for the aforementioned material properties were defined by [20, 21] through the use of iso-stress and iso-strain formulations for the characterization of fiber reinforced composites. The resulting formulations are:

$$E_x = V_f E_f + V_s E_s, \tag{d}$$

$$E_y = \frac{E_f E_s}{V_s E_f + \nu_f E_s}, \tag{e}$$

$$G_{xy} = \frac{G_f G_s}{V_s G_f + V_f G_s}, \tag{f}$$

$$\nu_{xy} = V_f \nu_f + V_s \nu_s\,, \tag{g}$$

$$\nu_{yx} = \nu_{xy}\frac{E_y}{E_x}, \tag{h}$$

where V_f, E_f, G_f, and ν_f are the volumetric fraction, elastic modulus, shear modulus, and Poisson's ratio of the embedded fibers, respectively, and V_s, E_s, G_s, and ν_s represent the same quantities for the elastic substrate. It is important to note that these approximations represent upper or lower bounds and should be experimentally verified when possible [20, 21].

In addition to knowledge of equations (3*a*)–(3*c*) and equations (d)–(h), formulation of the strain–displacement relationship must be established. Through examination of the elongation of a small element of the displaced membrane, as seen in figure 6 (top), the strain of the system in the x direction, and similarly in the y direction, due to lateral loads can be defined. Furthermore, by taking two linear elements as

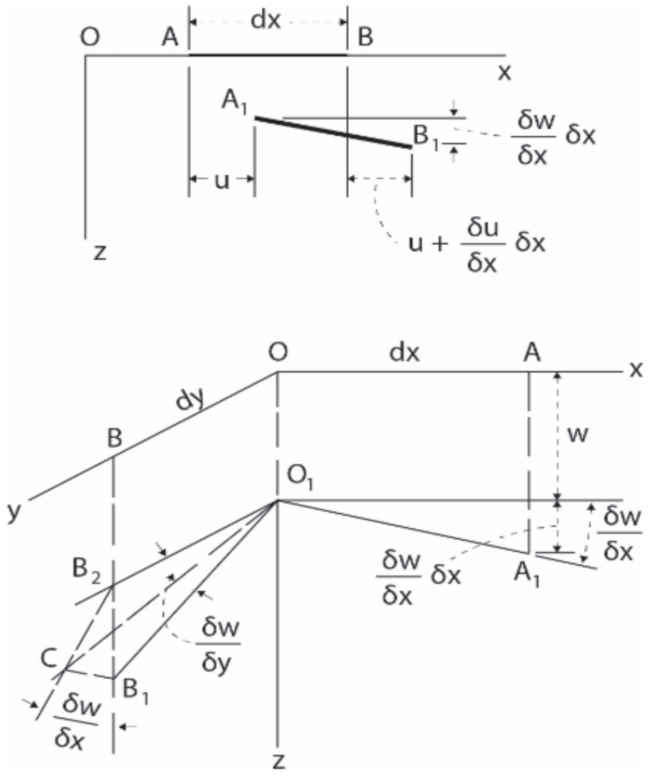

Figure 6. Depiction of axial strain ε_x due to displacement (top) and depiction of shear strain γ_{xy} due to displacement (bottom) (recreated from Timoshenko *et al* [17]).

seen in figure 6 (bottom), the shear strain can additionally be defined as follows:

$$\epsilon_x = \frac{\delta u}{\delta x} + \frac{1}{2}\left(\frac{\delta w}{\delta x}\right)^2, \tag{4a}$$

$$\epsilon_y = \frac{\delta v}{\delta y} + \frac{1}{2}\left(\frac{\delta w}{\delta y}\right)^2, \tag{4b}$$

$$\gamma_{xy} = \frac{\delta u}{\delta y} + \frac{\delta v}{\delta x} + \frac{\delta w}{\delta x}\frac{\delta w}{\delta y}. \tag{4c}$$

Equations (4*a*)–(4*c*) can then be used to define the compatibility condition:

$$\frac{\delta^2 \varepsilon_x}{\delta y^2} + \frac{\delta^2 \varepsilon_y}{\delta x^2} - \frac{\delta^2 \gamma_{xy}}{\delta x \delta y} = \left(\frac{\delta^2 w}{\delta x \delta y}\right) - \frac{\delta^2 w}{\delta x^2}\frac{\delta^2 w}{\delta y^2}. \tag{5}$$

Substitution of equations (3*a*)–(3*c*) and equations (a)–(c) into equation (5) then yields the reformulated Von Karman's equation (1) for a fiber reinforced composite material as:

$$\frac{1}{E_y}\frac{\delta^4 \phi}{\delta x^4} + \frac{1}{E_x}\frac{\delta^4 \phi}{\delta y^4} + \left(\frac{1}{G_{xy}} - \frac{\nu_{xy}}{E_x} - \frac{\nu_{yx}}{E_y}\right)\frac{\delta^4 \phi}{\delta x^4} = \left[\left(\frac{\delta^2 w}{\delta x \delta y}\right)^2 - \frac{\delta^2 w}{\delta x^2}\frac{\delta^2 w}{\delta y^2}\right], \tag{6}$$

where the right-hand-side of the equation is:

$$\left[\left(\frac{\delta^2 w}{\delta x \delta y}\right)^2 - \frac{\delta^2 w}{\delta x^2}\frac{\delta^2 w}{\delta y^2}\right] = -\frac{\pi^4 w_0^2}{32a^2b^2}\left[\cos\left(\frac{\pi x}{a}\right) + \cos\left(\frac{\pi y}{b}\right)\right]. \tag{i}$$

With the establishment of equation (6), the PDE can then be solved as a boundary value problem in order to determine the stress function $\Phi(x, y)$. The boundary conditions, defined by the condition of simply supported edges on rollers, were specified as the following:

1. $u(\pm a, y) = \pm\frac{1}{2}u_0$,
2. $v(x, \pm b) = \pm\frac{1}{2}v_0$,
3. $\tau_{xy}(\pm a, y) = 0$, and
4. $\tau_{yx}(x, \pm b) = 0$,

where u_0 and v_0 are the maximum displacements in the x and y directions, respectively. Due to the constant boundary conditions of (1) and (2), as well as the relationship between the shear stress and the derivatives $\frac{\delta u}{\delta y}$ and $\frac{\delta v}{\delta y}$ as seen in equation (4*c*), the boundary conditions (3) and (4) result in the following two equivalent conditions as specified in [17]:

$\frac{\delta v}{\delta x}(\pm a, y) = 0$,
$\frac{\delta u}{\delta y}(x, \pm b) = 0$.

In order to solve for the stress function $\Phi(x, y)$, particular and homogenous equations are solved for by assuming the following forms:

$$\phi_p(x, y) = c_1 \cos\left(\frac{\pi x}{a}\right) + c_2 \cos\left(\frac{\pi y}{b}\right), \tag{j}$$

$$\phi_h(x, y) = c_3 x^2 + c_4 y^2. \tag{k}$$

The particular solution, $\Phi_p(x, y)$, is solved for by substitution of equation (j) into equation (6) and solving for the unknown coefficients c_1 and c_2. This yields:

$$c_1 = -\frac{E_y a^2 w_0^2}{32b^2} \quad c_2 = -\frac{E_x b^2 w_0^2}{32a^2}. \tag{l}$$

The particular solution is then used to solve for the homogenous solution through the application of the boundary conditions. Using equations (3*a*)–(4*c*) and (a)–(c). The derivatives $\frac{\delta u}{\delta x}$ and $\frac{\delta v}{\delta y}$ can be expressed in terms of the stress function:

$$\frac{\delta u}{\delta x} = \frac{1}{Ex}\left(\frac{\delta^2 \phi}{\delta y^2} - \nu_{xy}\frac{\delta^2 \phi}{\delta x^2}\right) - \frac{1}{2}\left(\frac{\delta w}{\delta x}\right)^2, \tag{7a}$$

$$\frac{\delta v}{\delta y} = \frac{1}{Ey}\left(\frac{\delta^2 \phi}{\delta x^2} - \nu_{yx}\frac{\delta^2 \phi}{\delta y^2}\right) - \frac{1}{2}\left(\frac{\delta w}{\delta y}\right)^2. \tag{7b}$$

Integration of equations (7*a*) and (7*b*), with respect to x and y, respectively, and subsequent differentiation, with respect to y and x, respectively, allows for the application of the boundary conditions. Additionally, through the use of the particular solution, the unknown coefficients c_3 and c_4 are solved as:

$$c_3 = \frac{-1}{64a^2b^2(\nu_{xy}\nu_{yx}-1)}[E_y(\pi^2a^2w_0^2 + 16v_0a^2b) + E_x\nu_{yx}(\pi^2b^2w_0^2 + 16u_0ab^2)],$$
$$c_4 = \frac{-1}{64a^2b^2(\nu_{xy}\nu_{yx}-1)}[E_y\nu_{xy}(\pi^2a^2w_0^2 + 16v_0a^2b) + E_x(\pi^2b^2w_0^2 + 16u_0ab^2)]. \quad \text{(m)}$$

The complete stress function can then be formulated as:

$$\phi_p(x, y) = -\left[\frac{E_ya^2w_0^2}{32b^2}\cos\left(\frac{\pi x}{a}\right) + \frac{E_xb^2w_0^2}{32a^2}\cos\left(\frac{\pi y}{b}\right) + x^2\left(\frac{E_y(\pi^2a^2w_0^2 + 16v_0a^2b) + E_x\nu_{yx}(\pi^2b^2w_0^2 + 16u_0ab^2)}{64a^2b^2(\nu_{xy}\nu_{yx}-1)}\right) + y^2\left(\frac{E_y\nu_{xy}(\pi^2a^2w_0^2 + 16v_0a^2b) + E_x(\pi^2b^2w_0^2 + 16u_0ab^2)}{64a^2b^2(\nu_{xy}\nu_{yx}-1)}\right)\right]. \quad (8)$$

The displacement functions $u(x, y)$ and $v(x, y)$ are then determined from the stress function as:

$$u(x, y) = \frac{u_0x}{2a} + \frac{\pi w_0^2}{32a}\left[1 + \cos\left(\frac{\pi y}{b}\right) + \frac{\nu_{xy}E_ya^2}{E_xb^2}\right]\sin\left(\frac{\pi x}{a}\right), \quad (9)$$

$$v(x, y) = \frac{v_0y}{2b} + \frac{\pi w_0^2}{32b}\left[1 + \cos\left(\frac{\pi x}{a}\right) + \frac{\nu_{yx}E_xb^2}{E_ya^2}\right]\sin\left(\frac{\pi y}{b}\right), \quad (10)$$

forming the complete formulation of the membrane deformation with displacement $w(x, y)$:

$$w(x, y) = w_0\cos\frac{\pi x}{2a}\cos\frac{\pi y}{2b}. \quad (11)$$

With the establishment of the x-axis and y-axis displacements, the minimization of the mechanical potential energy within the membrane, also known as the energy methods [17, 18], is used to determine the overall deformation of the FPAM. The energy of the membrane is composed of three components. These components are the work done by the applied pressure W_P, the work done by the applied force at the edges of the membrane W_F, and the change in strain energy V of the membrane due to the application of this pressure. Taking into account that the actuator is composed of two flat sheets, the potential energy of the system can then be written as:

$$\Pi = 2[V - W_p - W_F]. \quad (12)$$

The strain energy of the system is defined as,

$$V = \frac{1}{2}\iiint[\sigma_x\epsilon_x + \sigma_y\epsilon_y + \tau_{xy}\gamma_{xy}]dxdydz, \quad (n)$$

where the stresses σ_x, σ_y, and τ_{xy} are calculated by substitution equation (8) into equations (a)–(c), the strains ε_x, ε_y, and γ_{xy} are calculated by substitution of equations (9)–(11) into equations (4*a*)–(4*c*), and the integration is taken over the dimensions of a single sheet. The work done by the pressure is defined as:

$$W_P = \iint[Pw(x, y)]dxdy\iint\left[Pw_0\cos\frac{\pi x}{2a}\cos\frac{\pi y}{2b}\right]dxdy, \quad (o)$$

where once again, integration is taken over the dimensions of a single sheet. Lastly, the work done by the applied force at the loaded edges $x = \pm a$ is:

$$W_F = \iiint[\sigma_F\epsilon_x]dxdydz = F\left[\frac{\pi^2w_0^2}{32a} + \frac{Fu_0}{2}\right] \quad (p)$$

where σ_F is the stress caused by the force F at the loaded edges.

Utilizing the energy components defined in (n)–(p) and equation (12), the potential energy can then be minimized with respect to the unknowns w_0, u_0 and v_0 as follows.

$$\frac{\delta\Pi}{\delta u_0} = 0, \quad (q)$$

$$\frac{\delta\Pi}{\delta v_0} = 0, \quad (r)$$

$$\frac{\delta\Pi}{\delta w_0} = 0. \quad (s)$$

Equations (q)–(s) could then be solved to define the input pressure P as a function of contraction u_0 and force generation F. However, an adjustment had to be made in order to reflect the real world deformation of the actuator. The energy method predicts contraction in both the x- and y-axis directions due to input pressure, establishing the following relationship when the actuator has reached equilibrium (zero force generation),

$$v_0 = \frac{a}{b}u_0. \quad (t)$$

However, in actuality the actuator expands in the y-axis direction when pressurized. In order to account for this, the opposite of the relationship established in equation (t) $\left(v_0 = -\frac{a}{b}u_0.\right)$ was substituted into equation (12) resulting in a potential energy formulation with only the unknowns w_0 and u_0. The corrected energy formulation is then minimized with respect to w_0 and u_0 to establish a relationship between the input pressure P, the contraction u_0, and the force generated by the actuator F. In the elastic range, an analytic formula can be found to relate the input pressure, force, and contraction of the actuator. However, this is impossible to achieve in the nonlinear regime. Therefore, as previously mentioned, the elastic solutions method is used to determine the performance of the actuator. This is accomplished through the use of numerical software to approximate the maximum force and contraction of the actuator at various inputs pressures through an iterative process. The differential potential energy equations (q), (s) in the elastic range are used as a first approximation. Subsequently, a nonlinear model, $E_x(\varepsilon_x)$ for the Young's Modulus in the x-axis direction is substituted for E_x. Utilizing the average strain in the x-axis direction as the input to the nonlinear model, an iterative approximation of the maximum actuator contraction and force generation of the FPAM is found.

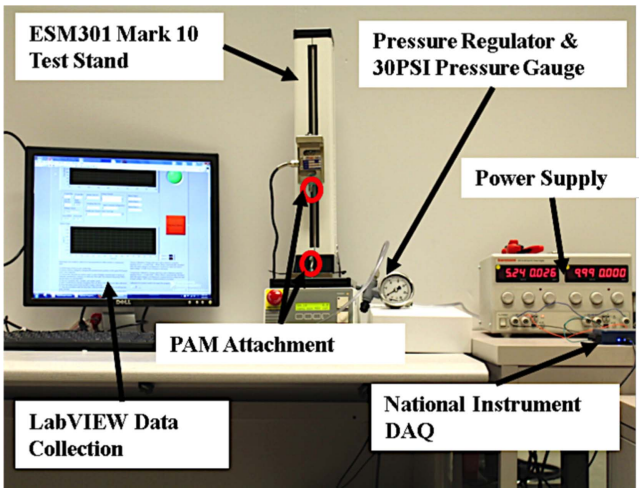

Figure 7. Diagram of experimental apparatus used to conduct force and contraction experiments.

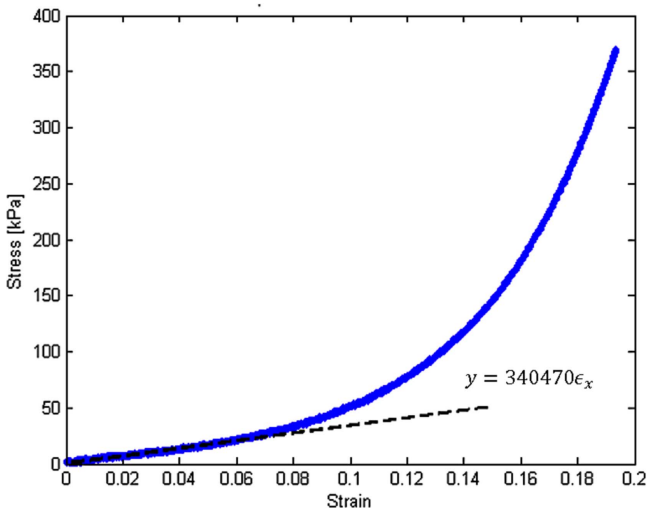

Figure 8. Experimental stress–strain relationship of FPAM up to 20% strain.

4. Experimental validation

An experimental apparatus was created to measure the mechanical performance of the FPAM (SCU & MCU). As seen in figure 7, the experimental setup is composed of a motorized test stand (ESM301, Mark-10) capable of providing single-axis distance measures, a single-axis load cell (STL-50, AmCells), a pressure gauge and regulator, a data acquisition unit (USB-6000, National Instruments), and a LabVIEW program designed to collect force and time data.

Prior to experimentation, the FPAMs were cyclically loaded, figure 12, to 'train' the actuators. The training consisted of each FPAM being pretensioned to 0.5 N (chosen to minimize slack in embedded fibers, while also reducing effects on actuator performance), pressurized to 103 kPa (chosen to avoid failure), and then manually contracted and extended over the FPAM's max displacement (14.3%) at 103 kPa using the Mark-10 at a speed of 30 mm min^{-1}. This procedure was to ensure repeatable behavior by overcoming initial adhesive forces between the substrates and fibers (leftover from fabrication) in addition to providing some level of constant plastic deformation to the substrates and fibers. Subsequently, the experimental setup was used to conduct three separate procedures.

In the first procedure, figure 11, the FPAMs were held fixed at their rest length (contraction = 0), while the air chamber was pressurized from 0 to 151 kPa in increments of 6.89 kPa. At the start of this procedure the FPAMs were manually pretensioned to 0.5 N by the Mark-10. The LabVIEW data collection program and Mark-10 were then zeroed. Pressurization was then systematically applied in the aforementioned increments, allowing for the generated force of the actuators to reach a steady state value (5–10 s after pressurization) before the data was recorded. This process was then repeated to collect additional data points at each input pressure. In this manner, the maximum force generation of the actuator due solely to pressurization could be properly recorded.

In the second procedure, figure 10, the FPAMs were pressurized at no load (applied force = 0), and allowed to freely contract while the air chamber was pressurized from 151 to 0 kPa in increments 6.89 kPa. At the start of the procedure the FPAMs were placed on the Mark-10. The LabVIEW data collection program and Mark-10 were then zeroed. Subsequently, the Mark-10 was lowered to allow the actuators space to contract. Pressurization was then systematically applied in the aforementioned increments. At each increment, the test stand was raised until the LabVIEW program showed a minor increase in the force reading generated by the actuator. At this point, the Mark-10's displacement was recorded to provide values for the contraction of the actuators. In addition, calipers were used to provide secondary verification of the contraction readings. This process was then repeated to collect additional data points at each input pressure. In this manner, the maximum contraction of the FPAMs due solely to pressurization could be properly recorded.

In the final procedure, figure 9, the FPAMs were pressurized at their rest lengths (contraction = 0) then manually contracted to no load conditions (applied force = 0). At the start of this procedure, the FPAMs were preloaded to 0.5 N by the Mark 10. The LabVIEW program and the Mark-10 were then zeroed. Subsequently the FPAMs were pressurized and allowed to reach steady state values (5–10 s after pressurization) prior to being contracted at a speed of 10 mm min^{-1}. This procedure was conducted at pressures ranging from 0 to 151 kPa (FPAMs failed at 151 kPa) in increments of 17 kPa, in order to provide an example of the traditional unloading curve (force versus contraction at various pressure) for pneumatic actuators.

These three experimental procedures were conducted, in order to provide an accurate measure of the characteristic force generation and the maximum contraction within the pressure range. In addition, tensile tests were conducted to determine the effective tensile modulus E_x in the x-axis direction (figure 8). At the start of this test, the actuators were pretensioned to 0.5 N to minimize slack. The LabVIEW

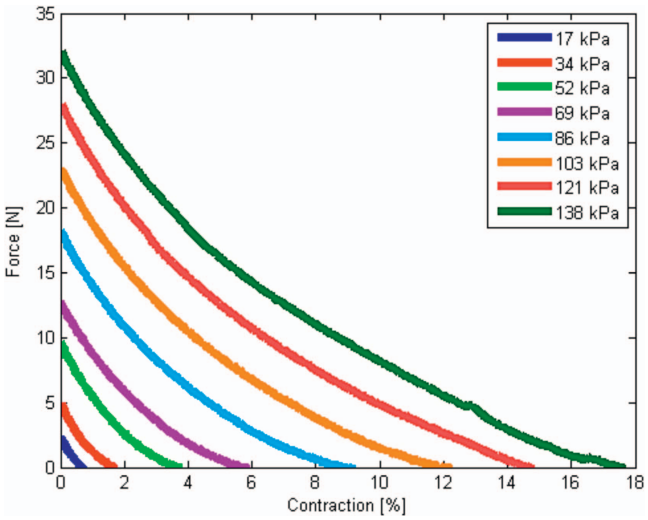

Figure 9. FPAM force–contraction relationship at pressures ranging from 0 to 138 kPa.

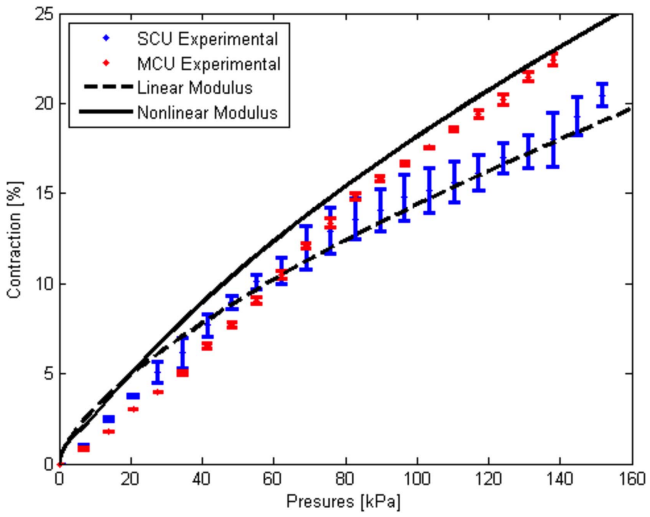

Figure 10. Maximum % contraction of FPAMs at pressures in the range of 0–157 kPa.

program and Mark-10 were zeroed. Subsequently the actuator was stretched at a rate of 10 mm min^{-1} from its initial pre-tensioned conditions. The tensile modulus was found to be linear up to about 5% strain, at which point the modulus increases until failure. The measured tensile modulus was found to be around 340 kPa, which is much lower than the 1.71 GPa calculated using the rule of mixtures found in equation (d). We believe this is due to how the fibers are oriented in the completed actuator. The Kevlar fibers were clamped at a single point at each end, which unevenly distributed stress along the fiber direction, and resulted in the occurrence of some slack. In addition, slippage between the Kevlar fibers and the silicone substrate during actuation also contributed to the smaller modulus. As such, the experimental tensile modulus was used to approximate the values for E_y, G_{xy}, ν_{xy}, and ν_{yx}, which were substituted into the model.

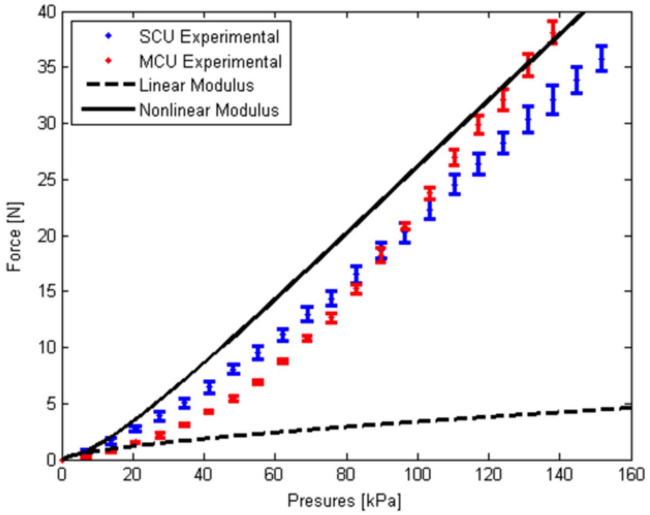

Figure 11. Maximum force of FPAM at pressures in the range of 0–157 kPa.

5. Results and discussion

Characterization of the FPAM's mechanical performance can be found in figure 9, which provides an example of the resulting force–contraction relationship of the SCU PAM up to 138 kPa (chosen to ensure actuators were not pushed to failure). Ultimately, through experimentation the SCU and MCU, the FPAMs were observed to fail at pressures around 150 kPa and 138 kPa, respectively. However, the failure mechanism that occurs is due to crack propagation, at high pressures, as the Kevlar fibers shear through the substrate, as opposed to delamination failure modes along the edges, which occurred more often and erratically in the previous design [16]. This is an improvement, as the observed failure mode can be accounted for in design and operation by setting a safety margin for input pressures. It is important to note that both the SCU and MCU have similar mechanical performances although the MCU failed more quickly than the SCU, as shown in figures 10 and 11. Additionally, an example of the repeatability of the results can be found in figure 12,

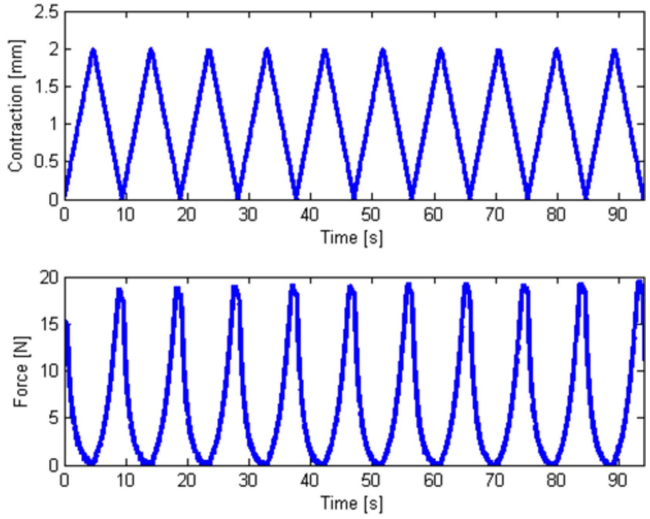

Figure 12. Cyclic loading of SCU at 103 kPa over a distance of 2 mm.

where the PAM reached a near constant force generation after 3–4 cycles at 103 kPa.

The SCU generated a maximum force of 35.7 ± 1 N and a maximum contraction of 20.5% ± 0.1% (2.87 ± 0.09 mm), while the MCU generated a maximum force of 38.1 ± 1 N and a maximum contraction of 22.4% ± 0.3% (9.42 ± 0.13 mm). The MCU, which is equivalent to three SCUs in series, was within 6.7% of the maximum force generation of the SCU and within 9.4% of thrice the maximum contraction of the SCU. The results are close to what would be expected in the ideal case despite the absence of inlet tubing between the three air volumes of the MCU design. This variation essentially adds an additional 12 mm to the deformable air volume, which may have affected the overall mechanical performance of the MCU. In addition, the larger form factor also affects the modulus of the MCU, when compared to that of the SCU, due to the increased interaction (contact forces) of the fibers and substrate between the fixed ends of the actuator. These issues, which will be addressed in future work through improved fabrication techniques, could be incorporated into the theoretical model for improved accuracy. This can be achieved by providing a new experimental modulus, as well as incorporating the additional 12 mm of deformable area as two additional air volumes of even size.

These experimental results were then compared to the theoretical model developed in this study. Both a linear and a nonlinear elastic moduli were utilized to numerically evaluate the theoretical model, due to our insight into the nature of the experimental procedures. During the contractile experiments, the deformation of the actuator remained in the elastic range as it was allowed to reach an equilibrium position, which resulted in near zero *x*-directional strain. However, during the force experiments, despite the fact that the actuator length was held fixed, the PAM still deformed in the *y*- and *z*-axis directions as a result of input pressure. These deformations resulted in *x*-directional strains, which incited a strain-hardening effect within the PAM. Ultimately, the strain-hardening effect lead to an increase in the force generated by the PAM. In order to incorporate this behavior into the model, an 8th order Ogden model (hyperplastic material model) was fit to the data in figure 8, and substituted into the model.

As can be seen in figure 10, both the linear and nonlinear modulus approximations performed admirably in predicting the contraction of the SCU to within ±0.67% and ±2.55% contraction, respectively. Both modulus approximations accurately capture the trajectory of the contraction response to pressure. Although the linear model seems to predict the behavior of the SCU slightly better in this case, it is due to the underperformance of the SCU caused by the rigid components, such as the inlet and the plug, which contributed to the prevention of full muscle contraction more in the SCU than in the MCU. In regards to the force response to pressure, shown in figure 11, only the nonlinear modulus was able to accurately predict both numerical values and trajectory of the experimental results. The theoretical model developed with the nonlinear modulus approximated the force generation of the SCU to within ±3.5 N, while the linear modulus predicted to within ±13.3 N. This error with the linear approximation was associated with the nonlinear behavior seen in the stress–strain relationship of the FPAM (figure 8). Overall, the development of the theoretical model with a nonlinear hyperelastic tensile modulus demonstrated high fidelity in approximating the performance of the actuators.

Further considerations for future work include the improvement of the mechanical performance of the presented actuator. The FPAM's maximum performance values, which are similar to that of other PAMs designed with embedded fibers [7, 16], are lower than those of traditional McKibben actuators [1, 2, 4, 5, 22] in general. However, this actuator is able to reach over 20% contraction with pressure inputs of 151 kPa, which is 2.5–5 times lower than the pressure inputs seen in the aforementioned McKibben actuators. As such, the FPAM is ideal for low pressure and low force applications, and will need to be customized through material selection for desired user tasks. For example, an increase in the *x*-directional modulus of the composite material will serve to increase the maximum force generated at the tested pressure ranges, while decreasing overall contraction and vice versa. Furthermore, the choice of base substrate can be chosen to reduce or increase the required pressure input for actuator deformation. Additionally, the slack within the fibers due to being clamped at a single point on both ends would need to be addressed. This design flaw served to reduce the overall force generated by the actuator within this study's experimental pressure range due to uneven stress distribution along the fiber strands. However, the fibers should be oriented and clamped in such a way as to evenly distribute the stress, reducing the ability of the fibers to slip through the substrate and allowing the material properties of the fibers and substrate to drive the FPAM's mechanical performance. In this manner, the fibers can be chosen with either higher or lower elastic moduli which would result in higher max forces and lower max contractions or lower max forces and higher max contractions in the applied pressure range respectively. Ultimately, the FPAM will be optimized for increased maximum contraction and force generation at similar pressure ranges used within this study.

In addition, the FPAM will be redesigned to incorporate embedded sensors. Due to the layered manufacturing process described, sensing capabilities can be easily added by altering the mold design to incorporate microchannels to be filled with a liquid conductor, such as eutectic gallium–indium (EGaIn) [23, 24], or by embedding a conductive soft polymer in an additional layer [13]. Subsequent experimentation with various microfluidic sensing designs such as those in [25–28] will need to be conducted in order to optimize actuator performance and sensing capability. However, the added advantage of embedded multi-modal sensing in the proposed 2D form factor will improve the FPAM's controllability, and thus the overall effectiveness of the FPAM. In addition, system identification to determine damping and spring coefficients at various pressures will need to be conducted. This will provide important information to improve the control of the FPAM, which is essential if it is to be used in a wearable orthotic or prosthetic device.

6. Conclusion

A simple fabrication technique was developed and employed to produce a 2D flat PAM. A theoretical model was developed to numerically predict the overall contraction and force generation of the actuator through the use of Von Karman's formulation for large deformations and the energy methods. Additionally, experimental analysis of the maximum force generation and contraction at various input pressures was used to characterize the mechanical performance of the flat PAM and to verify the fidelity of the theoretical model. Additionally, a theoretical model was developed and demonstrated accurate approximation of the mechanical properties of the PAMs to within 2.55% contraction and ±3.5 N force.

Acknowledgments

This work was sponsored in part by the GEM fellowship program, in part by Siemens (Award No.: A015580), and in part by Samsung (Award No.: A017519), whose supports are gratefully acknowledged. The authors would like to thank Dr Sung-Hwan Jang for his technical support with fabrication and Professor Carmel Majidi for his feedback in this study.

References

[1] Chou C and Hannaford B 1996 Measurement and modeling of McKibben pneumatic artificial muscles *Proc. IEEE Trans. Robot. Autom.* **12** 90–102

[2] Klute G K, Czemlecki J M and Hannaford B 1999 McKibben artificial muscles: pneumatic actuators with biomechanical intelligence *Proc. IEEE/ASME AIM (Atlanta, GA, USA)* pp 221–6

[3] Daerden F and Lefeber D 2002 Pneumatic artificial muscles: actuators for robotics and automation *Eur. J. Mech. Environ. Eng.* **47** 10–21

[4] Wakimoto S, Suzumori K and Kanda T 2005 Development of intelligent McKibben actuator with built-in soft conductive rubber sensor *Proc. IEEE Transducers* vol 1 *(Seoul, Korea)* pp 745–8

[5] Mizuno T, Tsujiuchi N, Koizumi T, Nakamura Y and Sugiura M 2011 Spring-damper model and articulation control of pneumatic artificial muscle actuators *Proc. IEEE ROBIO (Karon Beach, Thailand)* pp 1267–72

[6] Nakamura T and Shinohara H 2007 Position and force control based on mathematical models of pneumatic artificial muscles reinforced by straight glass fibers *Proc. IEEE ICRA (Roma, Italy)* pp 4361–6

[7] Park Y-L and Wood R J 2013 Smart pneumatic artificial muscle actuator with embedded microfluidic sensing *Proc. IEEE Sensors (Baltimore, MD, USA)* pp 689–92

[8] Bartlett N W, Tolley M T, Overvelde J T B, Weaver J C, Mosadegh B, Bertoldi K, Whitesides G M and Wood R J 2015 A 3D-printed, functionally graded soft robot powered by combustion *Science* **349** 161–5

[9] Shepherd R F, Stokes A A, Freake J, Barber J, Snyder P W, Mazzeo A D, Cademartiri L, Morin S A and Whitesides G M 2013 Using explosions to power a soft robot *Angew. Chem., Int. Ed. Engl.* **52** 2892–6

[10] Daerden F and Lefeber D 2001 The concept and design of pleated pneumatic artificial muscles *Int. J. Mech. Environ. Eng.* **2** 41–50

[11] Park Y-L, Chen B, Perez-Arancibia N O, Young D, Stirling L, Wood R J, Goldfield E C and Nagpal R 2014 Design and control of a bio-inspired soft wearable robotic device for ankle-foot rehabilitation *Bioinsp. Biomim.* **9** 016007

[12] Wakimoto S, Suzumori K and Kanda T 2005 Development of Intelligent McKibben actuator *Proc. IEEE/RSJ IROS (Edmonton, AB, Canada)* pp 487–92

[13] Kure K, Kanda T, Suzumori K and Wakimoto S 2008 Flexible displacement sensor using injected conductive paste *Sensors Actuators,* A **143** 272–8

[14] Felt W, Chin K Y and Remy C D 2015 Contraction sensing with smart braid McKibben muscles *IEEE/ASME Trans. Mechatron.* **21** 1201–9

[15] Erin O, Pol N, Valle L and Park Y-L 2016 Design of a bio-inspired pneumatic artificial muscle with self-contained sensing *Proc. IEEE EMBC (Orlando, FL, USA)* pp 2115–9

[16] Park Y-L, Santos J, Galloway K G, Goldfield E C and Wood R J 2014 A soft wearable robotic device for active knee motions using flat pneumatic artificial muscles *Proc. IEEE ICRA (Hong Kong, China)* pp 4805–10

[17] Timoshenko S and Woinowsky-Krieger S 1959 *Theory of Plates and Shells* 2nd edn (New York: McGraw-Hill) pp 378–87

[18] Timoshenko S and Woinowsky-Krieger S 1959 *Theory of Plates and Shells* 2nd edn (New York: McGraw-Hill) pp ISBN: 0-07-085820-9

[19] Lee T T 1961 Elastic-plastic analysis of simply supported rectangular plates under combined axial and lateral loading *PhD Dissertation* Fritz Laboratory Reports (Lehigh University)

[20] Campbell F C 2010 Introduction to composite materials *Structural Composite Materials* (Materials Park, OH: ASM International) pp 1–30

[21] Sideridis E 1988 The in-plane shear modulus of fiber reinforced composites as defined by the concept of interphase *Compos. Sci. Technol.* **31** 35–53

[22] Park Y-L, Chen B-R, Majidi C, Wood R J, Nagpal R and Goldfield E 2012 Active modular elastomer sleeve for soft wearable assistance robots *Proc. IEEE/RSJ IROS (Vilamoura, Algarve, Portugal)* pp 1595–602

[23] Dickey M D, Chiechi R C, Larsen R J, Weiss E A, Weitz D A and Whitesides G M 2008 Eutectic gallium–indium (EGaIn): a liquid metal alloy for the formation of stable structures in microchannels at room temperature *Adv. Funct. Mater.* **18** 1097–104

[24] Chiechi R C, Weiss E A, Dickey M D and Whitesides G M Eutectic gallium–indium (EGaIn): a moldable liquid metal for electrical characterization of self-assembled monolayers *Angew. Chem.* **120** 148–50

[25] Park Y-L, Majidi C, Kramer R, Bérard P and Wood R J 2010 Hyperelastic pressure sensing with liquid-embedded elastomer *J. Micromech. Microeng.* **20** 1–6

[26] Park Y-L, Chen B and Wood R J 2012 Design and fabrication of soft artificial skin using embedded microchannels and liquid conductors *IEEE Sens. J.* **101** 2711–8

[27] Mengüç Y, Park Y-L, Pei H, Vogt D, Aubin P, Fluke L, Winchell E, Stirling L, Wood R J and Walsh C J 2014 Wearable soft sensing suit for human gait measurement *Int. J. Robot. Res.* **33** 1748–64

[28] Shin H-S and Park Y-L 2016 Enhanced performance of microfluidic soft pressure sensors with embedded solid microspheres *J. Micromech. Microeng.* **26** 1–9